BNL-229493-2026-TECH

EIC-ADD-TN-160

Spin Diagnostics Using Mott Polarimeter for the EIC Pre-Injector

E. Wang

March 2026

Electron-Ion Collider

Brookhaven National Laboratory

U.S. Department of Energy

USDOE Office of Science (SC), Nuclear Physics (NP)

DISCLAIMER

Spin Diagnostics Using Mott Polarimeter for the EIC Pre-Injector

Erdong Wang

Brookhaven National Laboratory, Upton, NY 11973, USA

March 3, 2026

Abstract

Polarization measurement and front-end commissioning are critical steps in the EIC preinjector program. We designed a spin-diagnostics beamline at around 4 MeV for front-end commissioning. This paper describes a high-energy Mott polarimeter, including Mott scattering, the Sherman function, and extrapolation toward single elastic scattering in finite-thickness foils. We summarize the key equations used to calculate essential design parameters, including detection time, effective Sherman function, differential cross section, and Mott polarimeter figure of merit. We also present the diagnostics beamline lattice design and kicker design for continuous spin-polarization monitoring. These notes provide concepts, formulas, and methods for diagnostic-beamline design and commissioning measurements.

1 Introduction

The EIC preinjector front-end consists of a polarized electron source, a spin rotator, a bunching section, and a capture section [1]. The polarized electron source generates an electron beam with longitudinal spin orientation[2, 3, 4]. Wien filters are placed after the gun to rotate the spin from longitudinal to vertical. We measure polarization and spin direction after the spin rotator to confirm vertical spin orientation and to measure the polarization before injection into the linac. The spin-diagnostics beamline also measures beam energy and energy spread. Figure 1 shows the schematic layout of the EIC preinjector. We measure polarization after the L-band taper cavity, where the beam energy is around 4 MeV and the bunch energy chirp is removed.

Mott polarimetry measures the transverse polarization of electron beams through spin-orbit asymmetry in elastic Coulomb scattering from high-Z targets. For MeV-scale beams (3 MeV to 5 MeV kinetic energy), the single-scattering Sherman function remains appreciable at large back angles, while plural and multiple scattering in the target foil reduce the effective analyzing power. This manuscript summarizes the key formulas used to design, calibrate, and interpret measurements from a preinjector Mott polarimeter, and it discusses the current diagnostic beamline design.

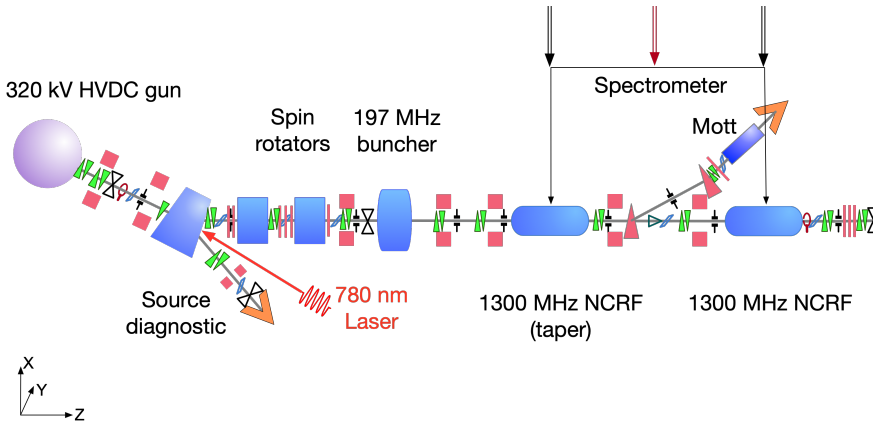

Figure 1: Schematic of the EIC preinjector front-end.

2 4 MeV Mott polarimeter

2.1 Mott polarimeter Physics

Consider an electron moving in the Coulomb field of a nucleus Ze. In the laboratory frame the nucleus produces an electrostatic field $\mathbf{E}(\mathbf{r}) = \dfrac{Ze}{r^3}\,\mathbf{r}$. In the instantaneous electron rest frame this electric field is seen as a magnetic field

$$\mathbf{B} = -\frac{1}{c}\,\mathbf{v} \times \mathbf{E}, \tag{1}$$

which couples to the electron magnetic moment $\boldsymbol{\mu}_s = -\dfrac{e}{mc}\,\mathbf{S}$. The interaction energy is

$$H_{\text{int}} = -\boldsymbol{\mu}_s \cdot \mathbf{B} = \frac{e}{mc}\,\mathbf{S} \cdot \frac{1}{c}(\mathbf{v} \times \mathbf{E}). \tag{2}$$

Using $\mathbf{L} = m\,\mathbf{r} \times \mathbf{v}$ and $\mathbf{E} \propto \mathbf{r}/r^3$, one obtains the spin-orbit potential

$$V_{\text{so}}(r) \simeq \frac{Ze^2}{2m^2c^2r^3}\,\mathbf{L} \cdot \mathbf{S}. \tag{3}$$

This spin-orbit term produces different scattering amplitudes for different spin states.

We follow Ref. [5, 6] to present the key equations of calculating the Mott scattering cross section and the most important parameter Sherman function.

The scattering of polarized electrons by a point nucleus is modeled using the partial wave expansion formulated by Sherman [5].

First, let's define a Coulomb parameter q:

$$q = \frac{\alpha Z}{\beta} \tag{4}$$

where $\beta = \frac{v}{c}$, E_k is the kinetic energy and α is the fine-structure constant. The Mott scattering uses two scalar amplitudes: a non-spin-flip amplitude $F(\theta)$ and a spin-flip amplitude $G(\theta)$, which are decomposed into an analytical Coulomb part (F_0, G_0) and the first order corrective terms (F_1, G_1):

$$F(\theta) = F_0(\theta) + F_1(\theta), \quad G(\theta) = G_0(\theta) + G_1(\theta) \tag{5}$$

The Coulomb terms are defined as:

$$F_0(\theta) = \frac{i\Gamma(1-iq)}{2\Gamma(1+iq)} \exp\left[iq \ln\left(\sin^2\frac{\theta}{2}\right)\right] \tag{6}$$

$$G_0(\theta) = -iq \cot^2\left(\frac{\theta}{2}\right) F_0(\theta) \tag{7}$$

Γ is the Gamma function. For stable and efficient numerical evaluation, the correction terms F_1 and G_1 use the Yennie–Ravenhall–Wilson transformation:

$$F_1(\theta) = \frac{i}{2} \sum_{k=0}^{n} \left[kD_k + (k+1)D_{k+1}\right] (-1)^k P_k(\cos\theta) \tag{8}$$

$$G_1(\theta) = \frac{i}{2} \sum_{k=0}^{n} \left[k^2 D_k - (k+1)^2 D_{k+1}\right] (-1)^k P_k(\cos\theta) \tag{9}$$

where P_k is the Legendre polynomial. The coefficients D_k are derived from the relativistic phase shifts:

$$D_k = \frac{e^{-i\pi k}\Gamma(k-iq)}{(k+iq)\Gamma(k+iq)} - \frac{e^{-i\pi\rho_k}\Gamma(\rho_k - iq)}{(\rho_k + iq)\Gamma(\rho_k + iq)} \tag{10}$$

where $\rho_k = \sqrt{k^2 - (\alpha Z)^2}$.

Finally, the differential cross-section $\frac{d\sigma}{d\Omega}$ and the Sherman function $S(\theta)$ are calculated as:

$$\frac{d\sigma}{d\Omega} = \lambda\!\!\!^{-2} q^2 (1-\beta^2) \left(|F|^2 \csc^2\frac{\theta}{2} + |G|^2 \sec^2\frac{\theta}{2}\right) \tag{11}$$

$$S(\theta) = \frac{2\lambda\!\!\!^{-2} q^2 (1-\beta^2)}{\sin\theta \left(\frac{d\sigma}{d\Omega}\right)} \mathrm{Re}\left\{F(\theta)G^*(\theta) + F^*(\theta)G(\theta)\right\} \tag{12}$$

where $\lambda\!\!\!^{-} = \frac{\hbar}{p} = \frac{\hbar c}{E\beta}$ is the de Broglie wavelength. The Sherman function depends on scattering angle. Tuning to the angle with maximum Sherman function yields maximum asymmetry, as shown in fig. 2. For a 4 MeV beam, the optimal scattering angle is 171.4° with a Sherman function of -0.522. We therefore place the Mott polarimeter detectors at this fixed angle. Over the 3–5 MeV range, the Sherman function remains high (about -0.504 to -0.522). The single-elastic-scattering cross section is shown in fig. 3.

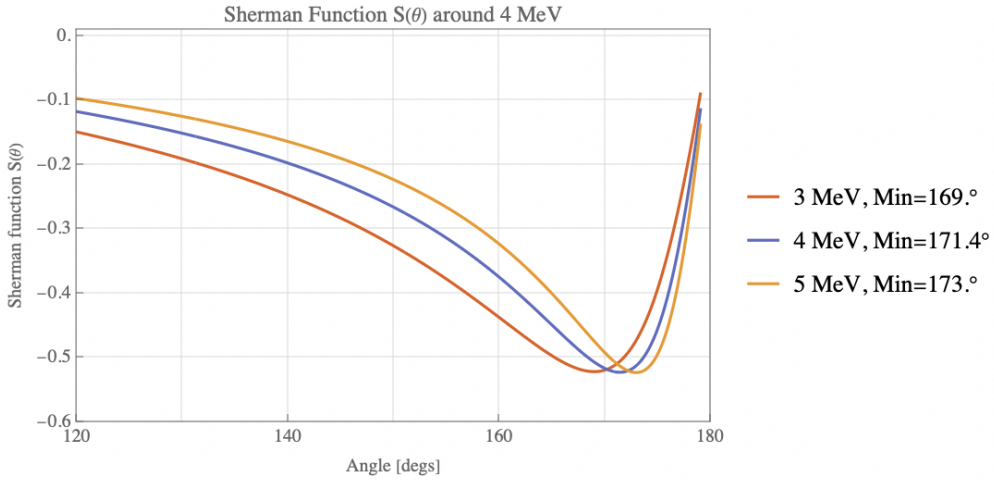

Figure 2: Single scattering Sherman function as the function of angle

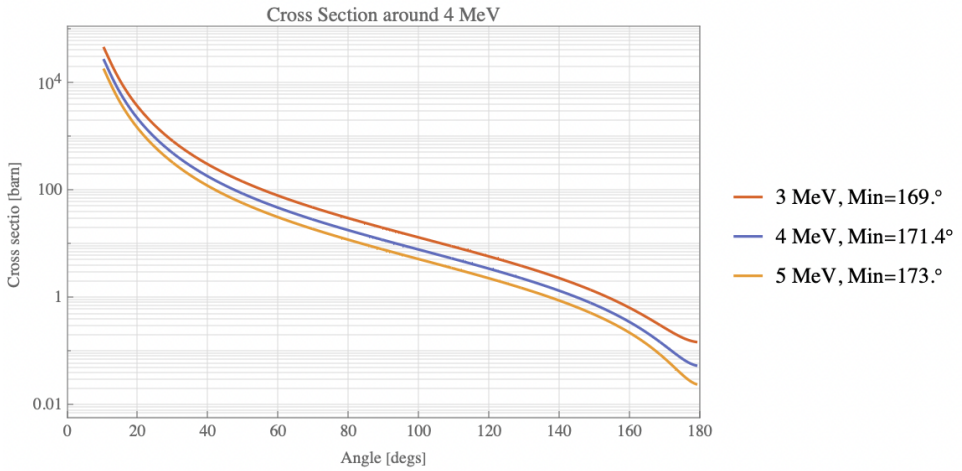

Figure 3: Single elastic scattering cross section

2.2 Scattering asymmetry measurement

2.2.1 Effective Sherman function, cross section and statistics

Three classes of corrections modify the idealized Coulomb Dirac solution: (i) atomic electron screening (important at low energies and forward angles), (ii) finite nuclear charge distribution (modifies large momentum transfer / back-angle scattering at higher energies), and (iii) radiative effects (bremsstrahlung, two-photon exchange) which are small at MeV energies. These effects can be simulated in the codes such as ELSEPA or Geant4[7].

Real targets are foils of finite thickness d. An electron traversing the foil may undergo zero, single, a few large-angle or many small-angle (multiple) scattering events. Only single large-angle elastic scattering from a nucleus produces the Sherman-function asymmetry given by the single-atom calculation. Multiple and plural scattering dilute the asymmetry in two ways: (a) electrons that undergo multiple small deflections add background without carrying the single-scattering analyzing power, and (b) electrons that scatter more than once can

have their spin-dependent correlations scrambled. Detailed determination of the Sherman function is discussed later. Here, we derive the optimal angle, detector rate, and single-scattering Sherman function.

A commonly used correction writes the measured (effective) Sherman function as

$$S_{\text{eff}}(\theta, d) \approx \frac{S_{\text{SA}}(\theta)}{1 + \alpha(E, \theta)\, d}, \tag{13}$$

where $S_{\text{SA}}(\theta)$ is the single-atom Sherman function and α is an empirical coefficient (depending on beam energy E, angle, and target material). The $1/(1 + \alpha d)$ form captures the leading dilution as foil thickness increases. Experimental studies at a few MeV have found α on the order of 0.2–0.4 μm^{-1} for Au at $\sim$5 MeV; e.g. $\alpha \approx 0.3/\mu\text{m}$ was reported in the Jefferson Lab Mott summary (Ref. [8]).

Given S_{eff}, the measured asymmetry(A) yields the beam polarization P via

$$P = \frac{A}{S_{\text{eff}}}. \tag{14}$$

Define detector solid angle $\Delta\Omega$ and detector efficiency η. The single-count rate for elastic scattering is

$$R = I_e\, n_t\, \sigma(\theta)\, \Delta\Omega\, \eta, \tag{15}$$

where I_e is the electron current, n_t is the areal density of scattering centers in the foil, $\Delta\Omega$ is the detector solid angle, and $\sigma(\theta)$ is the single-atom differential cross section. For an asymmetry measurement using two symmetric detectors (left/right), collecting N total counts from both arms, the statistical uncertainty on polarization is

$$\delta P \simeq \frac{1}{S_{\text{eff}}\sqrt{N}}. \tag{16}$$

To reach a target statistical precision δP_0 the required number of counts is

$$N \gtrsim \frac{1}{\left(S_{\text{eff}}\, \delta P_0\right)^2}, \tag{17}$$

and the measurement time is $T = N/R$. To achieve sufficient statistics, the detection time is

$$T = \left[\delta P^2 \left(\frac{\rho N_A}{M}\sigma(\theta)\Delta\Omega \cdot n_e d\right) \times \left(\frac{S_{\text{SA}}(\theta)}{1 + \alpha d}\right)^2\right]^{-1} \tag{18}$$

where δP is the uncertainty, d is the target thickness, and $\Delta\Omega$ is the detector solid angle. Figure 4 shows the time required to reach 0.5% uncertainty at various beam currents. For EIC operation, we use an average current of 36 nA. Methods to determine the Sherman function are discussed in the next section. Determining the single-scattering asymmetry A_0 requires extrapolation from measurements with multiple foil thicknesses, which takes time during commissioning. Once a reliable effective Sherman function is available, we can use a thicker target (e.g., 1 μm) and achieve this precision in about 30 minutes. The uncertainty requirement may be relaxed in future operation.

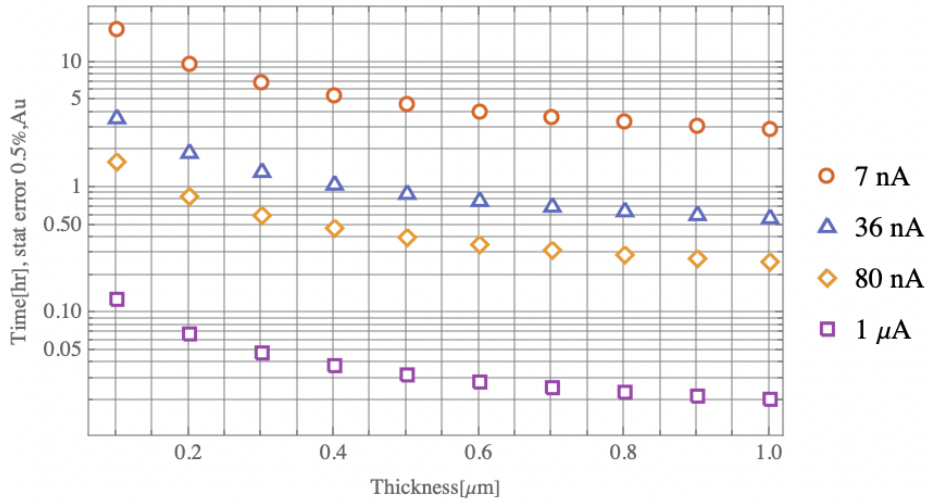

Figure 4: Detect time, assume stat error 0.5% and using Au as target at various beam current

The figure of merit (FoM) commonly used to optimize polarimeter settings is

$$\text{FoM} \equiv \sigma(\theta)\, S_{\text{eff}}^2(\theta, d), \tag{19}$$

which, up to beam current and detector efficiency factors, is proportional to the inverse time to reach given precision. The single scattering of FoM is shown in fig. 5a. With the target thickness, the Sherman function has to be replaced by the effective Sherman function and cross section has to include the thickness

$$\text{FoM}(d) = \left[\left(\frac{\rho N_A}{M}\sigma(\theta)\Delta\Omega\right)\cdot d\right] \times \left[\frac{S_{\text{SA}}(\theta)}{1+\alpha d}\right]^2 \tag{20}$$

then the FoM shows in the fig. 5b. The thicker target will give the shorter measurement time to achieve the same uncertainty.

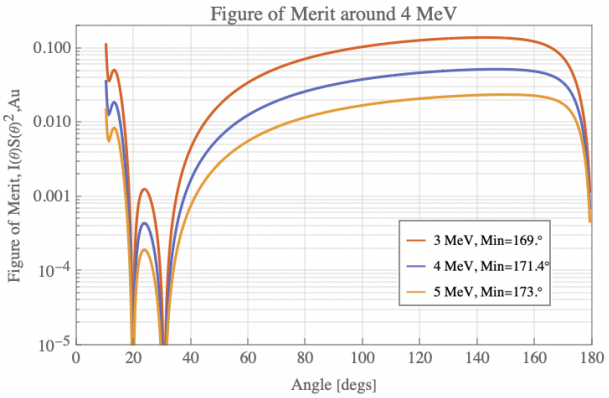

(a) Figure of merit for single scattering at various energies.

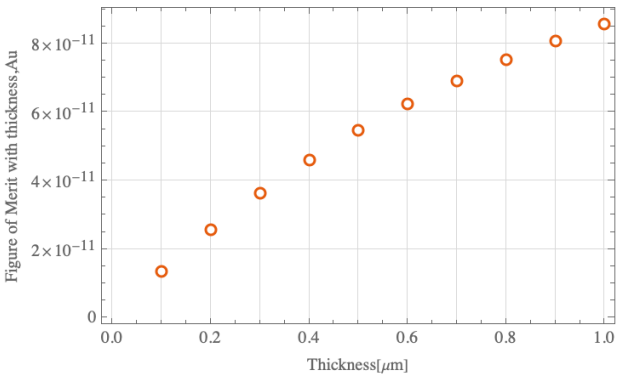

(b) Figure of merit for finite target thickness at the optimal scattering angle for 4 MeV

Figure 5: FoM of the Mott polarimeter.

Table 1: Summary of key design parameters of EIC Mott polarimeter

Parameter	**Symbol / Definition**	**Norminal Value[Range]**
Beam kinetic energy	E_k	$\sim 4\,\mathrm{MeV}$[3,5]
Optimal scattering angle	θ_{opt}	171.4°
Sherman function at θ_{opt}	$S(\theta_{\mathrm{opt}})$	-0.522 [-0.504, -0.522]
Effective Sherman model	$S_{\mathrm{eff}}(\theta, d)$	$\dfrac{S_{\mathrm{SA}}(\theta)}{1+\alpha d}$
Thickness-dilution coefficient (Au)	α	$\sim 0.3\,\mu\mathrm{m}^{-1}$ [0.2,0.4]
Cross section	$\dfrac{d\sigma}{d\Omega}$	0.109 b[0.061,0.244]
FoM definition	FoM	0.03 [0.016,0.062]
Target statistical uncertainty	δP	1% (example used in timing estimate)
Commissioning current	I_{com}	36 nA
Operation current	I_{opt}	1.2 nA
Operational target thickness	d	$\sim 1\,\mu\mathrm{m}$
Detector time	T	about 30 minutes (for commissioning)

2.2.2 Approaches to determine Sherman function

The methods used to determine the effective Sherman function in practice are listed as following. For the EIC, we will use the first two methods to determine the effective Sherman function and used to evaluate the polarization:

Thickness scan and extrapolation to single scattering. Measure asymmetry $A(d)$ for a set of target thicknesses d_i. Under a model such as Eq. (13), one fits $A(d) = P\,S_{\mathrm{eff}}(d)$ and extrapolates to $d \to 0$ to obtain $S_{\mathrm{SA}}(\theta)$ or directly determine S_{eff} at the chosen operational foil. This approach requires either a known beam polarization P or an independent reference. At the beginning of commissioning, we can use a theoretically calculated S_{SA} and extrapolated A_0 to estimate P.

The asymmetry can be measured using the following eq. (21), with $N\uparrow = \sqrt{L\uparrow R\uparrow}$, and $N\downarrow = \sqrt{L\downarrow R\downarrow}$. The $L\uparrow, R\uparrow, L\downarrow, R\downarrow$ are the Left and Right detector count of the spin up and down electrons

$$A = \frac{N\uparrow - N\downarrow}{N\uparrow + N\downarrow} \tag{21}$$

Simulation (Monte Carlo). Use detailed GEANT4 or ELSEPA simulations that include geometry, material properties, multiple scattering physics lists, detector responses, and energy cuts to compute the expected $S_{\mathrm{eff}}(d)$ curve and compare to data. This is essential to estimate model uncertainties when extrapolating. This method likely will be the most trustable method to determine the polarization after the first method.

Double-scattering (super-ratio) method. Use two successive analyzers (double scattering) in which the second stage analyzes a beam already scattered in the first stage. Properly arranged, this geometry can produce combinations of asymmetries that remove some systematic dependencies and give absolute sensitivity to S. Double-scattering experiments are technically more complex and are not always practical.

Benchmark with independent polarimeter or known source. If an independent, absolute polarimeter is available at similar beam energy, comparing simultaneous measurements yields S_{eff}. The 3-4 MeV Mott is the first polarimeter, it is not practical to the have an independent polarimeter at the same energy range. We have a source polarimeter, which can give a guideline, but not absolute value.

Later could consider combining two or three approaches yields the most robust Sherman function and constrains systematic errors.

2.3 Mott Hardware and detector setup

In the few-MeV regime, a Mott polarimeter must strongly suppress backgrounds because many more small-angle electrons are produced than the desired large-angle events, and detected electrons can include contributions from scattering on chamber hardware (walls, apertures, dump) in addition to the target foil. Energy alone is not a robust discriminator with plastic scintillators at these energies, and non-foil electrons can carry different asymmetry and bias/dilute the extracted polarization. Therefore, the polarimeter shall be designed to isolate elastic, foil-origin electrons using a combination of collimation, a two-layer scintillator detector, and time-of-flight (TOF) selection if the back scattering electrons from the beam dump can reach the detectors. The hardware set up discussed following is summarized from JLab 5 MeV Mott polarimeter with slightly changed for the geometry[8].

The polarimeter vacuum system comprises a scattering chamber containing the foil ladder and apertures, an extension section, and a long drift section ending in a light Z material beam dump such as aluminum/beryllium/copper. The foil ladder covers thicknesses from 100 nm to 1 µm, in 100 nm steps, giving 11 targets in total, plus an extra hole that allows the beam to go directly to the dump without scattering from a target. Internal aluminum liners upstream and downstream of the foils reduce backscattered electrons and photon backgrounds. The scattering chamber has four detector ports centered at a scattering angle of 171.4° and separated by 90° in azimuth (two horizontal and two vertical) to measure both transverse polarization components (polarization and spin direction) simultaneously. Each detector package includes lead and aluminum collimation followed by a thin ΔE scintillator (1.0 mm thick, 25.4 mm square) and a thick E scintillator (62.6 mm thick, 76.2 mm diameter) coupled to photomultipliers. The detector packages are surrounded by substantial lead shielding.

Online event definition is based on per-arm ΔE–E coincidence: discriminator outputs from the ΔE and E photomultiplier signals are combined in an AND to generate a coincidence for each arm, and the four arm coincidences are OR'ed to form the global trigger. A Mott electron deposits only a small energy in the ΔE scintillator (order 10 keV) and the remainder in the E scintillator, so the coincidence requirement preferentially selects charged particles traversing through both scintillator. Here the deposited energy is proptional to the scattering electron's energy and the the PMT tells the counts od how many events fall into

each energy bin. For each trigger, PMT waveforms are digitized by a 12-bit 250 MHz flash ADC; a pedestal is computed from pre-pulse samples and a pulse-area integral is formed to provide an energy-proportional observable in ADC units.

Residual backgrounds from the beam dump can be suppressed using TOF. The TOF spectrum of coincidence triggers shows a prompt peak from foil events and a later peak from electrons backscattered from the beam dump. In analysis, a timing window around the fitted foil peak (e.g., $\pm 2\sigma$) is applied to reject out-of-time backgrounds, and an energy window on the TOF-selected E spectrum is then used to count elastic events for the Mott asymmetry and polarization extraction.

2.3.1 Instrumental errors and measurement procedure

The main systematic uncertainties and practical mitigations are:

- Uncertainty of S_{SA} computation: Errors in the theoretical single-atom Sherman function from incomplete modeling (screening, nuclear form factor, radiative corrections). Mitigation: use modern partial-wave Dirac codes and cross-check between codes; uncertainties are typically $\lesssim 0.5\%$ for back angles at MeV energies.

- Target thickness and nonuniformity: Spatial thickness variation or pinholes change local S_{eff}. Mitigation: characterize foils (SEM, profilometry), choose high-quality evaporated films, and rotate/translate foils to average over inhomogeneities.

- Beam energy and energy spread: Sherman function and cross section depend on beam energy; energy loss in the foil modifies effective scattering energy. Mitigation: measure energy and spread with dispersive line; include energy loss in simulation.

- Detector acceptance and alignment: Finite detector size leads to averaging of $S(\theta)$ over an angular range; misalignment shifts central θ. Mitigation: precise mechanical alignment, collimation, and acceptance modeling in simulation.

- Backgrounds and accidental counts: Scattering from chamber walls, beam dump or bremsstrahlung may add events without spin asymmetry. Mitigation: shielding, time-of-flight cuts, ΔE vs E cuts, and background subtraction using off-target or dump-dominated spectra.

- Detector efficiency asymmetry and electronics dead time: Differences in left/right gain or time dependence of electronics can introduce false asymmetries. Mitigation: super-ratio methods, frequent helicity reversal, calibration pulser runs, and modern FADC readout that records pulses for offline reprocessing.

EIC error budgets for the polarimeter aim for total systematic uncertainty on S_{eff} at 1%. The following outlines a brief procedure for preinjector front-end commissioning:

1. Use Monte Carlo simulations and theoretical calculations to obtain the Sherman function and effective Sherman function.

2. Measure beam energy, energy spread, and charge with the dispersive diagnostic line.

3. Use a sequence of foil thicknesses to map $A(d)$ and compare with Monte Carlo predictions.

4. Use $S_{\text{eff}}(d)$ and S_{SA} for the operational foil to calculate polarization.

For routine operation, use the calibrated S_{eff} and choose foil thickness ($1\mu m$) that trades off acceptable measurement time versus foil lifetime.

For statistical planning, compute expected rates from the known beam bunch charge, repetition, foil areal density, single-atom cross section (from partial-wave codes or tables), detector solid angle and efficiency. Estimate run time required to reach target δP using eq. (18).

3 Diagnostics beamline design

3.1 Diagnostics beamline lattice

The spin-diagnostic beamline is placed between the L-band taper cavity and the capture cavity, where the beam energy is 3.5–4 MeV. It has multiple functions:

- Measure the beam energy
- measure the energy spread
- measure the spin direction and polarization
- Measure bunch charge and dump the beam for front-end beamline commissioning

To continuously observe spin-polarization changes, we design a kicker that extracts one bunch out of every 30 bunches. The kicker bends the beam by 15° to avoid beamline conflict with the next solenoid. To obtain sufficient dispersion for energy-spread measurements, we place another 15° dipole downstream, for a total bending angle of 30°. We design the diagnostic optics from the upstream solenoid. The initial beam parameters are obtained from Parmela tracking, listed in table 2

Parameter	**Value**
β_x	13.29 m
α_x	-11.36
β_y	19.73 m
α_y	-16.75
ϵ_n	6.54 mm-mrad
$\delta p/p$	2 %
E_k	3.8 MeV

Table 2: Initial beam parameters from the L-band taper cavity

The beamline optics use a flexible configuration that can switch between two primary operational modes: one optimized for Mott polarimetry to minimize beam size in both transverse directions, and one for energy-spread measurements to increase dispersion while reducing the beta function.

The lattice layout consists of an upstream solenoid, two bending dipoles, and two focusing quadrupoles arranged for dispersion control and beam-spot matching. This arrangement enables flexible tuning of dispersion and focusing for different diagnostic targets.

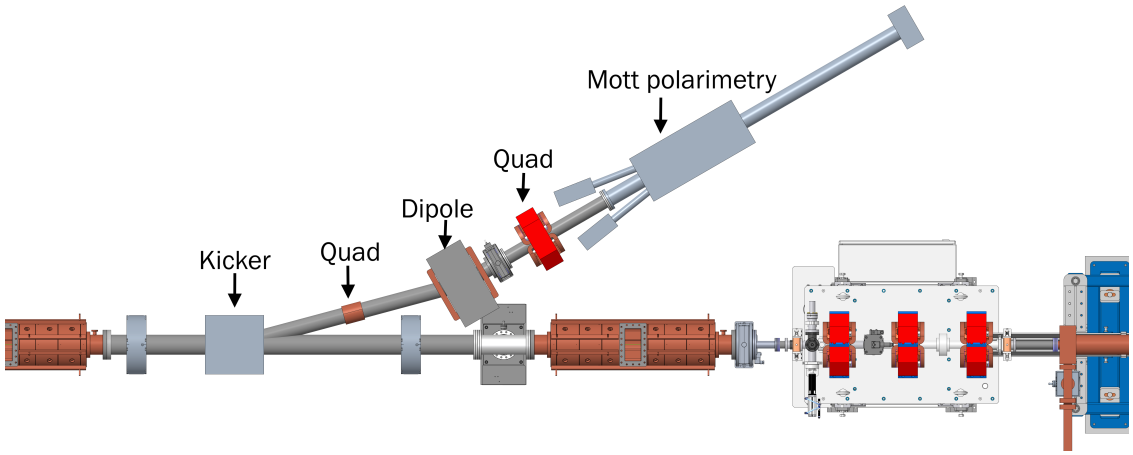

Figure 6: Layout of the spin diagnostic beamline showing the solenoid, kicker dipole, one quadrupole, static dipole and second quadrupoles.

For energy-spread measurements (dp/p), the lattice is tuned to minimize the betatron beam-size contribution while maximizing dispersion at a diagnostic screen located at $z = 2.45\,\mathrm{m}$. As shown in Figure 7, the lattice produces a beam waist (minimum β_x) at the screen location while maximizing horizontal dispersion (D_x). In this mode, the beam width is 88% from dispersion and 12% from transverse emittance.

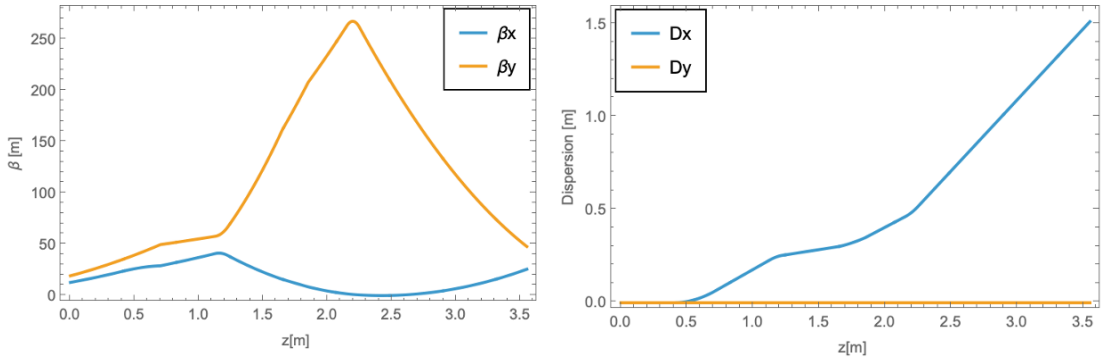

Figure 7: Lattice functions for the energy spread measurement mode. The plots show the minimization of the beta function and the maximization of dispersion at the diagnostic screen location ($z = 2.45$ m).

For spin polarization measurements via Mott scattering, the beam is transported to a

target located at $z = 3.6\,\mathrm{m}$. In this mode, the primary optical requirement is to produce a symmetric, round beam spot to minimize geometric systematic errors in the scattering asymmetry. The lattice is tuned such that the horizontal and vertical beta functions are equal and minimum at the target ($\beta_x \approx \beta_y$) as shown in Figure 8. The designed lattice controlled RMS beam size ($\sigma_x \approx \sigma_y$) suitable for the Mott target interaction.

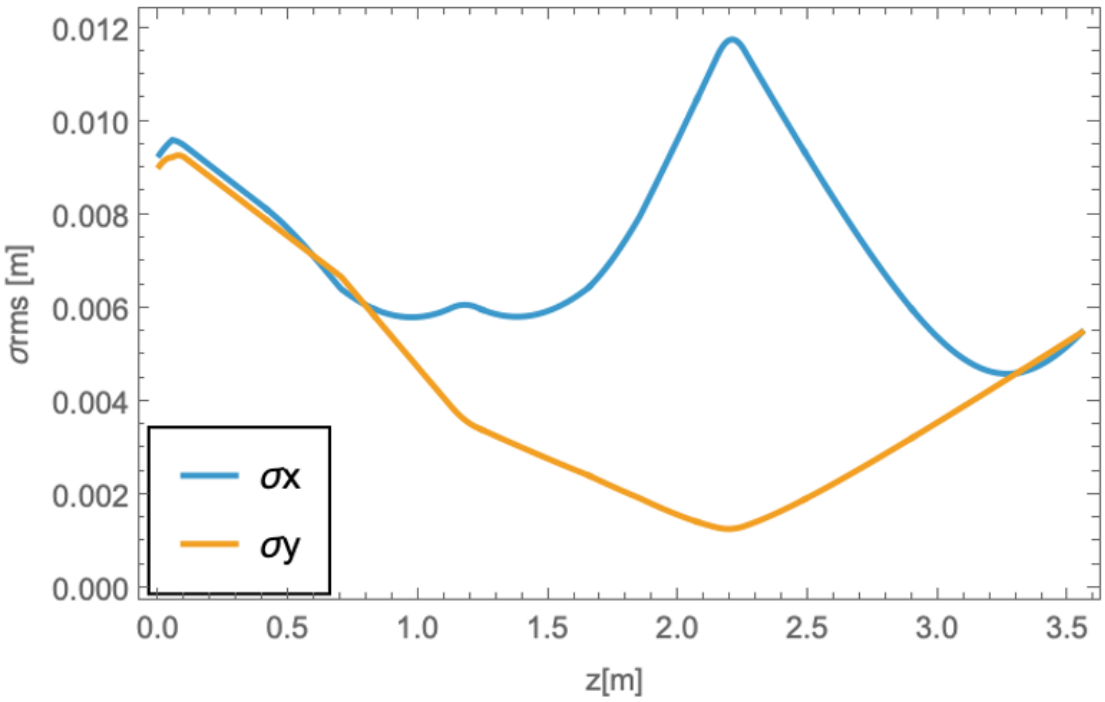

Figure 8: RMS beam size evolution along the beamline for the polarization measurement mode. The lattice is matched to provide a round beam ($\sigma_x \approx \sigma_y$) at the Mott target location ($z = 3.6$ m).

Table 3: Diagnostics Lattice

Element	**Energy spread**	**Spin Measurement**	**Element length**
Solenoid	0.0016(T)	0.1032 (T)	10 (cm)
Kicker	0.015 (T)	0.015 (T)	30 (cm)
Quad1	0.17(T/m)	0.1610 (T/m)	10 (cm)
Dipole	0.0186 (T)	0.0186 (T)	20 (cm)
Quad2	-0.12(T/m)	0.27 (T/m)	10 (cm)

3.2 Kicker consideration ,calculation and parameters choice

The preinjector operates at 30 Hz. The spacing between two bunches is about 30 ms. Therefore, we design a kicker with 10 ms rise/fall time and a flat-top shorter than 10 ms.

At this low frequency, a aircore magnetic kicker is practical and avoids the more complex vacuum design of a stripline kicker, similar as [9]. The design targets a uniform transverse magnetic field to preserve emittance and near-zero longitudinal field to avoid spin rotation. For a cylindrical surface of radius R, a surface current density $\vec{K}$ directed along the length (z-axis) with a cosine dependence on the azimuthal angle ϕ:

$$\vec{K}(\phi) = K_0 \cos(\phi)\hat{z} \tag{22}$$

generates a perfectly uniform magnetic field $\vec{B}$ inside the cylinder. Two common Cosine-Theta dipole magnet are evaluated and compared.

3.2.1 Canted Cosine Theta (CCT) dipole kicker

The CCT geometry generates a pure dipolar magnetic field by superimposing two solenoid windings that are canted in opposite directions. The design ensures that the longitudinal solenoidal field components cancel out, while the transverse dipolar components reinforce each other, resulting in a uniform transverse magnetic field suitable for the diagnostics beamline kicker.

The magnet geometry is defined by two counter-wound helical paths on a cylindrical surface slightly difference of the radius due to the wire thickness.The equations discussed here are following [10]

The geometry is governed by the following parameters:

- Magnet Radius: R
- Magnet Length: L
- Number of Turns: N
- Tilt Angle: θ_{tilt} (defined relative to the transverse plane)

The axial pitch per turn, h, is defined as:

$$h = \frac{L}{N} \tag{23}$$

The skew amplitude A, which determines the magnitude of the geometric modulation, is derived from the tilt angle:

$$A = \frac{R}{\tan(90^\circ - \theta_{tilt})} \tag{24}$$

The two windings are described by parametric equations $\vec{r}(t)$ where t ranges from 0 to $2\pi N$. The term $A\sin(t)$ introduces the canting. Two wires A has different sign Here is the coil

$$\vec{r} = \begin{cases} x(t) = R\cos(t) \\ y(t) = R\sin(t) \\ z(t) = \frac{L \cdot t}{2\pi N} \pm A\sin(t) - \frac{L}{2} \end{cases} \tag{25}$$

One coil radius is R, and another one is $R + \delta R$ due to larger radius for outside layer.

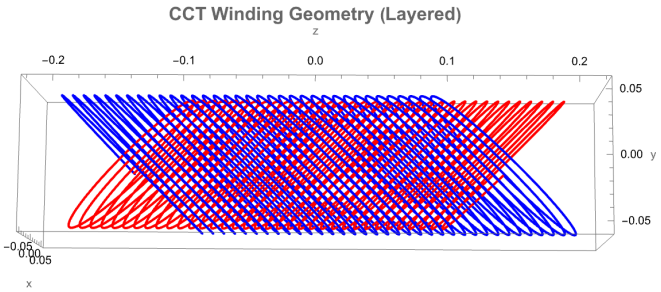

Figure 9: CCT Winding dipole geometry

The magnetic field $\vec{B}$ at any point $\vec{p}$ in space is calculated using the Biot-Savart Law. The current I flows through Coil 1, and $-I$ (opposite direction) flows through Coil 2.

For a single wire path $\vec{r}(t)$, the field is calculated by integrating the parametric form:

$$\vec{B}_{coil}(\vec{p}) = \frac{\mu_0 I}{4\pi} \int_0^{2\pi N} \frac{\frac{d\vec{r}}{dt} \times (\vec{p} - \vec{r}(t))}{|\vec{p} - \vec{r}(t)|^3} dt \tag{26}$$

where $\frac{d\vec{r}}{dt}$ is the tangent vector derivative with respect to the parameter t.

The total field is obtained by subtracting the contribution of the second coil from the first. The transverse and longitudinal field distributions are shown in fig. 10.

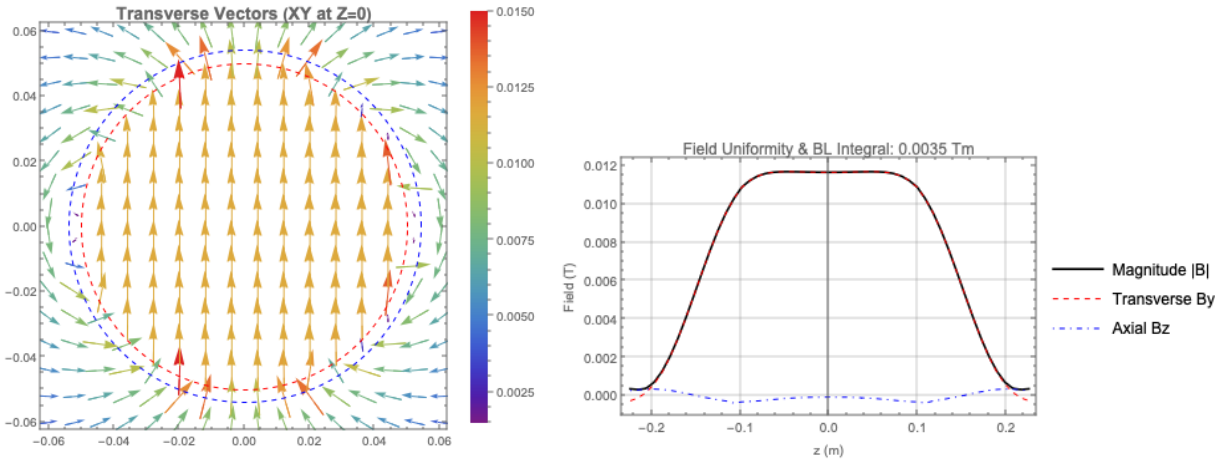

(a) Magnetic field at Z=0

(b) By and magnetic field intensity along the z axis

Figure 10: Simulated magnetic field profiles.

To obtain the inductance and evaluate current requirements for the desired rise and fall times, we first calculate the stored energy. The stored energy W is estimated by integrating the magnetic-energy density over the magnet bore volume V_{bore}.

$$W = \int_{V_{bore}} \frac{|\vec{B}|^2}{2\mu_0} dV \approx \frac{V_{bore}}{2\mu_0} \cdot \langle B^2 \rangle \tag{27}$$

Then, the inductance L_{ind} of the magnet is derived directly from the stored energy and

the operating current I:

$$L_{ind} = \frac{2W}{I^2} \tag{28}$$

The power supply voltage to drive this kicker is

$$V(t) = L\frac{di}{dt} + R \cdot i(t)$$

.

3.2.2 Cosine Theta Saddle Dipole kicker

The CCT is challenging to remove during vacuum-chamber bakeout. At the polarized-gun test beamline, we developed correctors based on the Cosine Theta Saddle (CTS), which can provide a uniform dipole field. Here we evaluate whether CTS can also be used as a kicker. We approximate the distribution by placing N discrete turns at specific angular positions θ_k.

To maintain the field uniformity, the positions of the wires must be chosen such that the cumulative current distribution matches the integral of the cosine function. The integrated current I_{cum} up to a height y is proportional to:

$$y(\theta) = R\sin(\theta) \tag{29}$$

Therefore, to approximate the cosine distribution with discrete wires carrying equal currents, the wires should be spaced uniformly in the projected height y.

Then the angular position of the k-th turn (where $k = 0 \ldots N-1$) is:

$$\theta_k = \arcsin\left(\frac{k+0.5}{N}\right) \tag{30}$$

In this evaluation, we assume the wire has zero thickness, so the return wire is overlapped. We also do not include bedstead edges, though they may be used in fabrication to approximate a hard-edge field.

- Magnet Radius: R
- Magnet Length: L
- Number of Turns: N

The magnet consists of N loops in the upper half-plane ($y > 0$) and N symmetric loops in the lower half-plane ($y < 0$). The lower loops carry current in the same sense (constructive interference) to double the field magnitude at the center. The magnet radius is R and Length is L. The magnet geometry is shown in fig. 11

The magnetic field B at any point in space generated by a single coil is calculated using the Biot–Savart law in eq. (26). The total field is the sum of the fields generated by each coil. The transverse and longitudinal field distributions are shown in fig. 12.

The magnetic stored energy and inductance are calculated using eq. (27) and eq. (28).

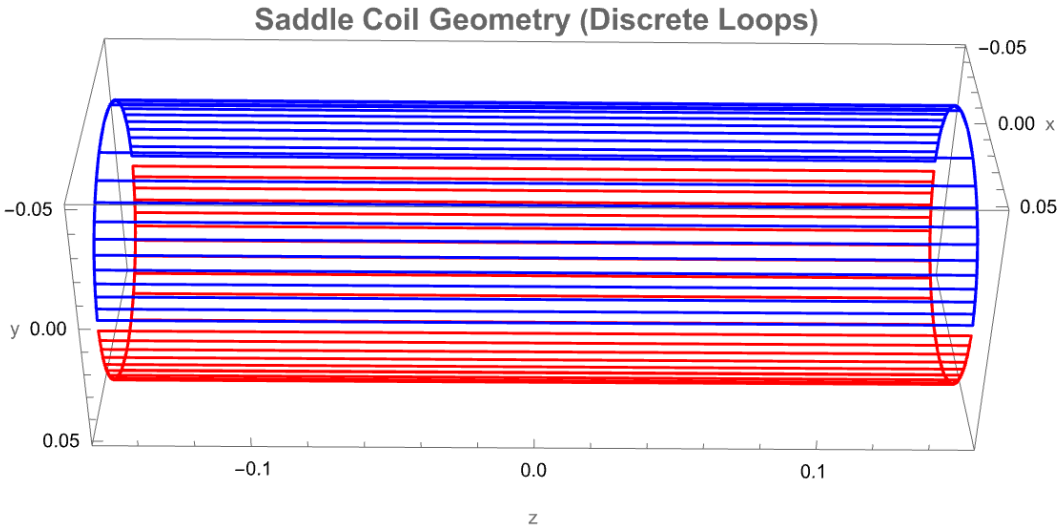

Figure 11: CTS Winding dipole geometry

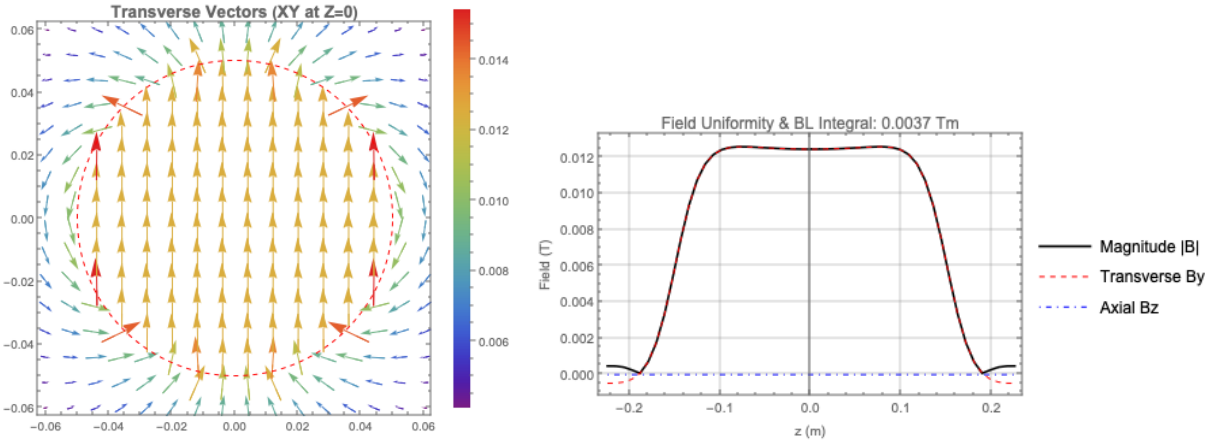

(a) Magnetic field at Z=0

(b) By and magnetic field intensity along the z axis

Figure 12: Simulated magnetic field profiles.

3.2.3 Parameters Table and Selection

The following table summarizes the parameters of CCT and CTS kicker using the above equations. The geometry parameters are used to draw fig. 9 and fig. 11

Table 4: Comparison of CTS and CCT Simulation Parameters

Parameter	**Unit**	**CTS**	**CCT**
Beam Parameter			
Kinetic Energy	MeV	3.8	
Target Bending Angle	deg	15	
Pulse Length	ms	10	
Rise/drop Time	ms	< 10	
Rep. rate	Hz	1	
Error (pk-pk)	%	< 0.3	
Required Field Integral (BL)	T·m	≈ 0.0037	
Kicker Main Parameters			
Magnet Radius (R)	m	0.05	0.05
Magnet Length (L)	m	0.30	0.30
Turns per Layer (N)	-	11	35
Tilt Angle	deg	NA	45
Tuned Current (Inner)	A	86.28	75.82
Tuned Current (Outer)	A	NA	76.45
Simulated Bz Integral	T·m	0	7.2×10^{-6}
Inductance (Est)	H	0.000025	0.000038
Stored Energy (Est)	J	0.0921	0.073
Total Wire Length	m	17.61	≈ 22.0

The additional voltage required to ramp the current can be estimated by $L\frac{di}{dt}$. Using table 4, the extra voltage is 0.096 V for CTS and 0.141 V for CCT. Both values are small.

Comparing the CTS and CCT kicker configurations, CTS has the following advantages:

1. The Bz integral is much smaller than in CCT.
2. It requires only one power supply because all coils carry the same current.
3. It is easier to remove from the beam pipe for bakeout.

Therefore, we select the CTS structure as the diagnostic beamline kicker.

4 Conclusion

This document discusses the design of the preinjector spin-diagnostic beamline. We provide an explicit derivation of the Mott-scattering amplitudes, their connection to the Sherman function used in polarimetry, and practical corrections for plural and multiple scattering in

finite foils. This technote presents a concept for the EIC preinjector spin-diagnostic beamline and a 4 MeV-class Mott polarimeter for front-end commissioning. It summarizes the key formulas for Mott geometry, statistical measurement time, Sherman function, polarization extraction, and figure of merit in practical operation. It also presents the detector concept, background-mitigation approach, and measurement procedure. The diagnostics beamline lattice is presented, including kicker, optics, viewers, and beam dump. To enable near-continuous polarization monitoring during commissioning, a low-frequency CTS kicker is evaluated to extract periodic bunches into the diagnostic line.

Acknowledgements

The author acknowledges discussions with J. Grames, M. Bruker and R. Suleiman regarding the EIC Mott polarimeter design.

References

[1] Erdong Wang, John Skaritka, Jyoti Biswas, and Vahid Ranjbar. The design progress of a high charge low energy spread polarized pre injector for Electron Ion Collider. pages 114–117 pages. JACoW Publishing, July 2024.

[2] Erdong Wang. Space charge effects on spin polarization in high-intensity preinjector. Technical Report BNL–226378-2024-TECH, EIC-ADD-TN-113, 2478783, November 2024.

[3] Jyoti Biswas, Erdong Wang, Omer Rahman, John Skaritka, Adam Masters, Sylvain Marsillac, and Tai-De Li. Polarized Photocathode R&D at BNL and spin consideration for the EIC. In *Proceedings of 20th International Workshop on Polarized Source, Targets, and Polarimetry — PoS(PSTP2024)*, page 026, Jefferson Lab, Newport News, VA, February 2025.

[4] Erdong Wang, Omer Rahman, Jyoti Biswas, John Skaritka, Patrick Inacker, Wei Liu, Ronald Napoli, and Matthew Paniccia. High-intensity polarized electron gun featuring distributed Bragg reflector GaAs photocathode. *Applied Physics Letters*, 124(25):254101, June 2024.

[5] Noah Sherman. Coulomb scattering of relativistic electrons by point nuclei. *Physical Review*, 103(6):1601–1607, 1956.

[6] X. Roca-Maza. Theoretical calculations for precision polarimetry based on Mott scattering. *Europhysics Letters*, 120(3):33002, February 2018.

[7] J. Allison, K. Amako, J. Apostolakis, P. Arce, M. Asai, T. Aso, E. Bagli, A. Bagulya, S. Banerjee, G. Barrand, B. R. Beck, A. G. Bogdanov, D. Brandt, J. M. C. Brown, H. Burkhardt, Ph. Canal, D. Cano-Ott, S. Chauvie, K. Cho, G. A. P. Cirrone, G. Cooperman, M. A. Cortés-Giraldo, G. Cosmo, G. Cuttone, G. Depaola, L. Desorgher, X. Dong, A. Dotti, V. D. Elvira, G. Folger, Z. Francis, A. Galoyan, L. Garnier,

M. Gayer, K. L. Genser, V. M. Grichine, S. Guatelli, P. Guèye, P. Gumplinger, A. S. Howard, I. Hřivnáčová, S. Hwang, S. Incerti, A. Ivanchenko, V. N. Ivanchenko, F. W. Jones, S. Y. Jun, P. Kaitaniemi, N. Karakatsanis, M. Karamitros, M. Kelsey, A. Kimura, T. Koi, H. Kurashige, A. Lechner, S. B. Lee, F. Longo, M. Maire, D. Mancusi, A. Mantero, E. Mendoza, B. Morgan, K. Murakami, T. Nikitina, L. Pandola, P. Paprocki, J. Perl, I. Petrović, M. G. Pia, W. Pokorski, J. M. Quesada, M. Raine, M. A. Reis, A. Ribon, A. Ristić Fira, F. Romano, G. Russo, G. Santin, T. Sasaki, D. Sawkey, J. I. Shin, I. I. Strakovsky, A. Taborda, S. Tanaka, B. Tomé, T. Toshito, H. N. Tran, P. R. Truscott, L. Urban, V. Uzhinsky, J. M. Verbeke, M. Verderi, B. L. Wendt, H. Wenzel, D. H. Wright, D. M. Wright, T. Yamashita, J. Yarba, and H. Yoshida. Recent developments in Geant4. *Nuclear Instruments and Methods in Physics Research Section A: Accelerators, Spectrometers, Detectors and Associated Equipment*, 835:186–225, November 2016.

[8] J. M. Grames, C. K. Sinclair, M. Poelker, X. Roca-Maza, M. L. Stutzman, R. Suleiman, Md. A. Mamun, M. McHugh, D. Moser, J. Hansknecht, B. Moffit, and T. J. Gay. High precision 5 MeV Mott polarimeter. *Physical Review C*, 102(1):015501, July 2020.

[9] V Tioukine, K Aulenbacher, and C Matejcek. Kicker-magnet for the 5.0 MeV polarimeter at MESA. 2023.

[10] D.I. Meyer and R. Flasck. A new configuration for a dipole magnet for use in high energy physics applications. *Nuclear Instruments and Methods*, 80(2):339–341, April 1970.